FULL PAPER

A Three-Dimensionally Interconnected Carbon Nanotube–Conducting Polymer Hydrogel Network for High-Performance Flexible Battery Electrodes

Zheng Chen, John W. F. To, Chao Wang, Zhenda Lu, Nan Liu, Alex Chortos, Lijia Pan, Fei Wei, Yi Cui,* and Zhenan Bao*

High-performance flexible energy-storage devices have great potential as power sources for wearable electronics. One major limitation to the realization of these applications is the lack of flexible electrodes with excellent mechanical and electrochemical properties. Currently employed batteries and supercapacitors are mainly based on electrodes that are not flexible enough for these purposes. Here, a three-dimensionally interconnected hybrid hydrogel system based on carbon nanotube (CNT)-conductive polymer network architecture is reported for high-performance flexible lithium ion battery electrodes. Unlike previously reported conducting polymers (e.g., polyaniline, polypyrrole, polythiophene), which are mechanically fragile and incompatible with aqueous solution processing, this interpenetrating network of the CNT-conducting polymer hydrogel exibits good mechanical properties, high conductivity, and facile ion transport, leading to facile electrode kinetics and high strain tolerance during electrode volume change. A high-rate capability for TiO_2 and high cycling stability for SiNP electrodes are reported. Typically, the flexible TiO_2 electrodes achieved a capacity of 76 mAh g^{-1} in 40 s of charge/discharge and a high areal capacity of 2.2 mAh cm^{-2} can be obtained for flexible SiNP-based electrodes at 0.1C rate. This simple yet efficient solution process is promising for the fabrication of a variety of high performance flexible electrodes.

1. Introduction

High-performance, lightweight, flexible energy-storage devices such as batteries and supercapacitors are potential power sources for wearable devices, artificial electronic skins, distributed sensors and other portable electronics.[1–4] To translate such potentials into reality, one major task is to develop flexible electrodes with reliable mechanical properties and excellent electrochemical performances. To realize good mechanical properties, the electrodes should possess strong interaction with the current collector (if applied) or hold a robust scaffold that can sustain mechanical abuse. To achieve high electrochemical performance, the electrodes need to preserve efficient ionic and electronic conductivity during electrode operation. Unfortunately, currently employed batteries and supercapacitors are mainly based on relatively rigid and fragile electrodes and are unsuitable for flexible device fabrication because they suffer from structural failure when deformed or folded.[5–7]

To address this problem, effort has being devoted to designing new structures to render the electrodes flexible. The most common approaches for fabricating flexible electrodes is to directly coat electrode slurries containing active materials, carbon and binder on flexible substrates such as plastic,[4,8] textile[9–11] or paper.[3,5] While this approach is both simple and efficient, it utilizes substantial amount of inert

Dr. Z. Chen, J. W. F. To, Dr. C. Wang, Dr. N. Liu, A. Chortos, Prof. Z. Bao
Department of Chemical Engineering
Stanford University
Stanford, CA 94305, USA
E-mail: zbao@stanford.edu
Dr. Z. Lu, Prof. Y. Cui
Department of Materials Science and Engineering
Stanford University
Stanford, CA 94305, USA
E-mail: yicui@stanford.edu
Prof. L. Pan
National Laboratory of Microstructures (Nanjing)
School of Electronic Science and Engineering
Nanjing University
Nanjing 210093, China

Prof. F. Wei
Department of Chemical Engineering
Tsinghua University
Beijing 100084, P. R. China
Prof. Y. Cui
Stanford Institute for Materials and Energy Sciences
SLAC National Accelerator Laboratory
Menlo Park, CA 94205, USA
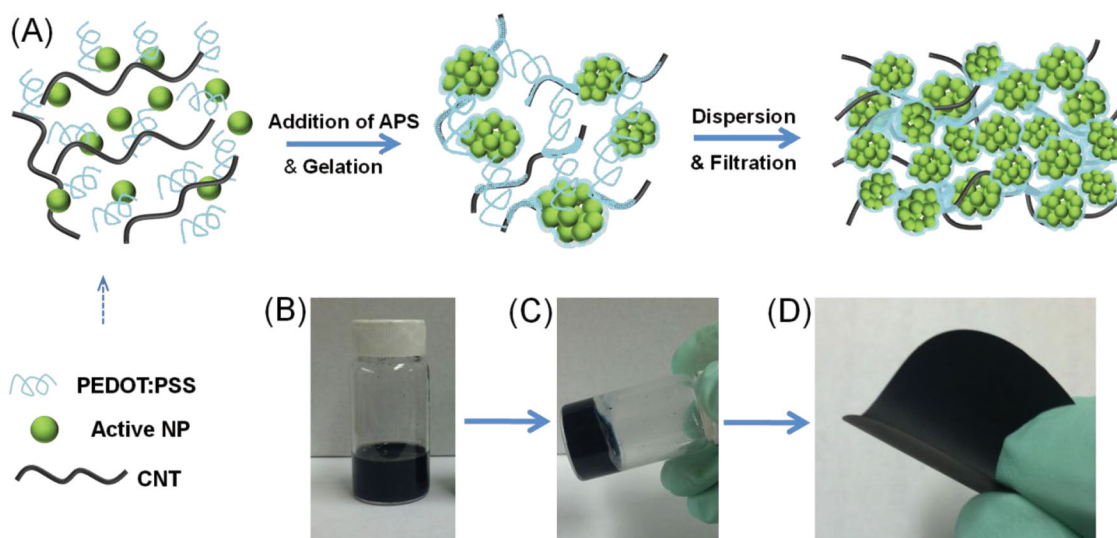
Figure 1. A) Schematic of the aqueous solution process to fabricate flexible electrodes using active nanoparticles (e.g., TiO$_2$ or Si nanoparticles), CNT and PEDOT:PSS. B) Photograph of the precursor solution containing TiO$_2$ nanoparticles, CNT and PEDOT:PSS; the existence of PEDOT:PSS significantly enhanced the dispersion of CNT and improved the homogeneity of the dispersion (Figure S1, Supporting Information). C) Photograph of a composite hydrogel composed of TiO$_2$ nanoparticles, CNT and PEDOT:PSS. D) Photograph of an example of a flexible TiO$_2$-PEDOT:PSS-CNT film fabricated using the above-described solution process.

components that inevitably compromise the device's volumetric and gravimetric energy density. More importantly, for plastic substrates the effective control of the interface between the substrate and active layer remains to be developed; for textile and paper, the active materials may be embedded inside a porous network but their stability in organic electrolyte remains an issue. On the other hand, conducting polymers (CPs) such as polyaniline, polypyrrole and their derivatives, have shown great promise to afford light-weight, flexible electrodes. However, most electrochemically active CPs again suffer from mechanical brittleness, low capacity (<150 mAh g^{-1}) and poor chemical or electrochemical stabilities.[12] Therefore, flexible electrodes made from CPs is dependent upon its substrate for mechanical robustness and, hence, have only a moderate cycling lifetime.[13–17] Furthermore, even though single cable-based devices are flexible and mechanically robust, but the total charge capacity of the entire device is too low (measured at only a few mF cm^{-2} or µAh cm^{-2}) for practical usage.[6,18,19]

Another versatile approach toward achieving flexible electrodes is to enable flexible nanocomposite films by filtering solutions containing nanosized active materials and carbon nanotubes (CNTs) or graphene.[20–22] In such films, the active materials offer charge capacity, while the CNTs or graphene provides both electronic conductivity and mechanical support. However, surface functionalization of CNTs and graphene are required to enable solution processing, hence affecting the electronic conductivity. Thin electrodes made from such composite architectures showed impressive charge storage performances, while thicker electrodes made with the same structure often hold a significantly decreased capacity at increased charge/discharge rate, which is attributed to a rapid increase of contact resistance from the CNT or graphene junctions. By using either CNT or graphene only, one can make high-rate flexible supercapacitors with reasonable mass loading, but the charge capacity from CNT or graphene is double-layer capacitive in nature, and

is insufficient for high-energy devices.[23,24] In summary, the challenge to effectively fabricate flexible electrodes for high-performance electrochemical energy devices still remains.

2. Results and Discussions

Here, we report a simple yet efficient aqueous solution process to fabricate high-performance flexible electrodes using materials comprised of interpenetrating networks of CNT and conducting polymer hydrogel. As illustrated in **Figure 1**A, we started with a homogenous precursor solution containing water-stable conducting polymer, namely poly(3,4-ethylenedioxythiophene) doped with poly(4-styrenesulfonate) (PEDOT:PSS), super-long (diameters of 30–80 nm and length of up to 1 mm) CNT and electrochemically active nanoparticles. The CNTs are found to be well dispersed in the aqueous solution containing PEDOT:PSS (Figure 1B). Addition of gelation agents (e.g., ammonium persulfate (APS)) promoted the composite solution to form a hydrogel (Figure 1C) in about 5 min. The as-formed gel was then re-dispersed by adding more deionized (DI) water with stirring. Subsequent vacuum filtration condensed the hydrogel networks into highly robust and flexible freestanding composite films, which can then be peeled off and cut into desired size and shape for lithium-ion cell fabrication.

In the matrix, the super-long CNT creates as an ideal scaffold with high mechanical robustness and long-range conductivity. Our control experiment using multiwalled CNTs (diameters of 30–80 nm, length of 20–30 µm) failed to produce a freestanding, flexible film with a similar loading of active nanoparticles, which indicates that longer CNT is essential to ensure mechanical robustness of the composite film. Electrochemically active nanoparticles were chosen from a vast library of recently reported energy storage system.[25,26] With factors such as low cost, abundance and environmental friendliness, we chose

www.MaterialsViews.com

ADVANCED
ENERGY
MATERIALS
www.advenergymat.de

FULL PAPER

commercially available TiO_2 and Si nanoparticle (SiNP) to demonstrate high-rate and stable lithium-ion battery, respectively. Additionally, water-soluble PEDOT:PSS was used because it has a conjugated backbone that allows efficient transport of de-localized electrons through the π orbital systems, leading to high electronic conductivity (10–1000 S cm^{-1}),[27,28] which is ideal for electrode applications. In contrast, most of the other CPs have lower electronic conductivity and are difficult to process in aqueous solution due to their low solubility.[12,29] Moreover, the PSS can enhance the dispersion of CNT in water, presumably through non-covalent stabilization due to a polymer "wrapping" mechanism where the hydrophobic part of the polymer chain covers the CNT surface and the polar hydrophilic part interacts with water to dissociate the CNT bundles.[30] The significantly improved CNT dispersion using PEDOT:PSS can be clearly observed by comparing with another dispersion in which no PEDOT:PSS was present (Figure S1, Supporting Information). A better dispersion provides more uniform distribution of CNT in the composite film, resulting in better mechanical property and higher conductivity. At the same time, nanoparticles that were dispersed in water tend to form numerous aggregates (or clusters) due to van der Waals forces or electrostatic interactions.[31] Such nanoparticle clusters can be then easily wrapped by the dispersed PEDOT:PSS, again due to hydrophobic-hydrophilic interactions. The subsequent gelation process, initiated by electrostatic interaction between cations, e.g. NH_4^+, and negatively charged PSS, stabilizes the conducting polymer-CNT network where polymer-wrapped nanoparticle clusters are embedded within. Filtration processes further strengthens such composite network and creates a 3D interconnected conductive hydrogel-CNT architecture with outstanding electrical and mechanical properties (Figure 1C).

We should also mention that previous work on PEDOT:PSS/CNT composites focused mainly on thin films (<1 μm) for photovoltaic applications.[32] Although a thick PEDOT:PSS/CNT film was used, its specific charge capacity was too low due to the device's small charge capacity from both PEDOT:PSS and CNT.[33] In contrast, our hydrogel approach allows us to process significantly more complicated systems by incorporating a variety of active materials, leading to a CNT-conducting polymer hydrogel network structure with critical features that have not been achieved before. These include: i) the long CNT scaffold provides global electron transport pathways and excellent mechanical robustness; ii) the conducting polymer provides high local conductivity by minimizing contact resistance from nanoparticles and CNTs; iii) the entangled network of CNTs and polymers synergistically provides excellent mechanical robustness and high conductivity which otherwise cannot be achieved without polymer wrapping; iv) the effective incorporation of electrochemically active particles significantly increases the charge capacity; and v) the network structure creates interconnected channels for effective ion transport and small nanoparticles offer short solid-state diffusion length. These advantageous characteristics have allowed us to fabricate thick, flexible electrodes with high mechanical robustness and high electrochemical activity.

TiO_2 nanoparticles were first used as an active material to fabricate high-rate flexible lithium electrodes. Anatase TiO_2 has been studied as a promising electrode material for safe lithium storage due to its moderate voltage window.[25] Recent studies

suggest that significant pseudocapacitive effect occurs on nanoparticulate or mesoporous TiO_2 due to increased surface effect compared with bulk structures, which dramatically increase the rate performance. However, such an effect can only be maintained within thin film electrodes due to the low conductivity of TiO_2 (10^{-3} to 10^{-8} S cm^{-1}).[34–37] Nevertheless, our water-based synthetic strategy allowed us to successfully fabricate flexible thick TiO_2 composite electrodes (TiO_2-PEDOT:PSS-CNT) with high rate capability and high areal capacity.

Figure 2A shows a representative scanning electron microscopy (SEM) image of the flexible TiO_2-PEDOT:PSS-CNT film, which exhibits a network structure formed by interpenetration of long CNTs and PEDOT:PSS. The composition of the film can be easily tuned by simply varying the ratio of each constituent; in which we have focused on a composition of 57%-TiO_2, 28%-CNT and 15%-polymer (by weight) for this work. Although porous features can be clearly recognized, the film is relatively dense due to the filtration and polymer wrapping. Numerous TiO_2 nanoparticle clusters are surrounded by CNT network, forming intimate interfaces with each other. Figure 2B shows the cross-sectional SEM image of the film, indicating a film thickness of ≈20 μm. According to the areal mass loading (2.8 mg cm^{-2}), the average density of the film is ≈1.4 g cm^{-3}. It corresponds to a porosity of ≈45% for the composite. This packing density is significantly higher than P25 (0.108 g cm^{-3}) and meso-TiO_2 (0.714 g cm^{-3}), as reported previously.[38] Such a high density is consistent with the surface topography shown in Figure 2A. A high-resolution SEM image of a selected area in the cross section reveals a unique multilayered structure where CNTs were stretched out from the network (Figure 2C). We note that large CNT bundles were not observed from the cross-sectional images, which further confirms the facile dispersion of CNT with the aid of PEDOT:PSS. In addition, the obtained transmission electron microscopy (TEM) image (Figure 2D) clearly shows the TiO_2 clusters penetrated by CNTs. Closer observation using TEM (Figure 2E and Supporting Information Figure S2) clearly shows the effective coating of PEDOT:PSS on the surface of TiO_2 particle. To further elucidate how the PEDOT:PSS interacts with CNT and TiO_2, elemental mapping was performed using scanning transmission electron microscopy (STEM) energy-dispersive X-ray (EDX) spectroscopy technique. As shown in Figure 2F, the distribution of CNT, TiO_2 and PEDOT:PSS is indicated by C-K, Ti-K and S/C-K mapping, respectively. The uniform distribution of each element suggests that PEDOT:PSS were wrapped on the TiO_2 surface and have penetrated through the CNT network. Thus, the effective CNT-polymer hydrogel network and conducting wrapping have provided thick electrodes with desired electrical and mechanical properties.

To enable flexible electrode applications, it is important to correlate the electrical and mechanical properties of the composite film. Direct measurement of the conductivity using 4-point probe shows a high conductivity of 215 S cm^{-1} for the TiO_2-PEDOT:PSS-CNT film. This conductivity is only slightly lower than that of the PEDOT:PSS-CNT film (measured at 950 S cm^{-1}), as made by a similar process, since a large fraction (57 wt%) of TiO_2 nanoparticles were incorporated into the conductive network. To investigate the relationship between electrical and mechanical properties, the resistance of a typical TiO_2-PEDOT:PSS-CNT film was monitored under
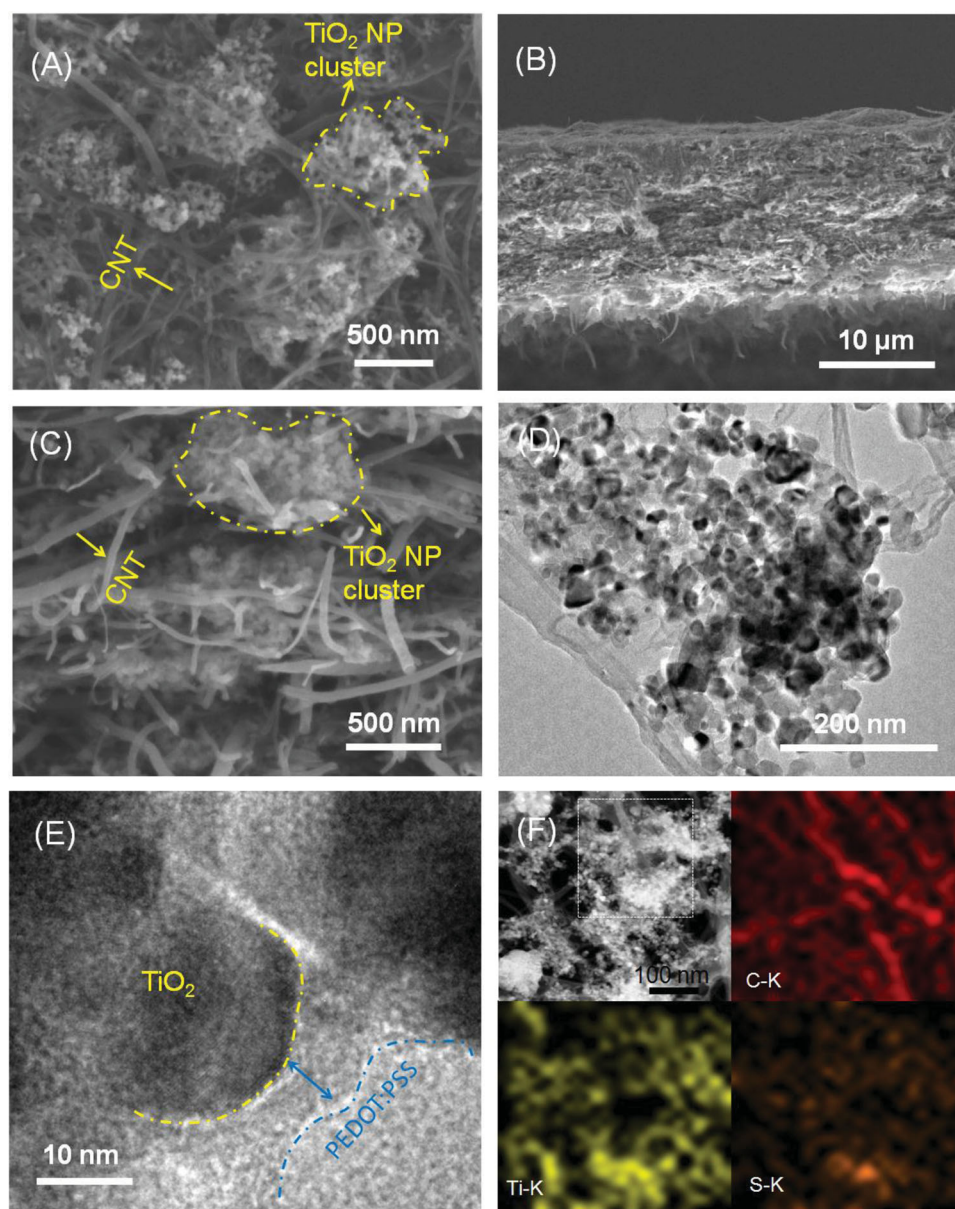
Figure 2. A) SEM image of the surface view of a representative TiO_2-PEDOT:PSS-CNT film electrode. The CNT network penetrates through the whole film and TiO_2 NPs form clusters that are embraced by CNT pathways. B) Low and C) high magnification SEM images of the cross-section view of the TiO_2-PEDOT:PSS-CNT film electrode. A typical film has a thickness of ≈20 μm. The CNT backbones can be clearly observed. D) TEM image of the composite film showing a typical TiO_2 cluster and the CNT network. E) TEM image showing the wrapping of PEDOT:PSS on the surface of a TiO_2 particle. F) Elemental mapping showing the distribution of CNT, PEDOT:PSS and TiO_2 nanoparticles (up-left: spectrum image scanning, up-right: C-K mapping, bottom-left: Ti-K mapping, bottom-right: S-K mapping)

different bending conditions. **Figure 3**A shows a film under a bending radius of 2.0 mm, which illustrates its superior flexibility. While the resistance of the film was stable under slight bending (radius >4.5 mm), we observed that further bending of the film resulted in decreased resistance. As shown in Figure 3B, the film resistance decreased by ≈8% as the bending radius was decreased from 4.5 to 2.0 mm. This could be due to better contacts in the compressed polymer-CNT network upon bending. In addition, our electrode film was constructed by the superlong CNT entanglement and polymer wrapping. The PEDOT:PSS can easily wrap around the CNT junctions due to

capillary force, which prevents the CNT separation and retains conductivity during bending. Furthermore, this film is highly robust under repeated bending cycles. As shown in Figure 3C, the film resistance shows negligible change after 500 bending cycles at a bending radius of 3.5 mm, indicating its good overall mechanical property.

The highly conductive, robust CNT-polymer network provides the TiO_2 electrodes with superior rate performance. To characterize the electrochemical performance, the TiO_2-PEDOT:PSS-CNT electrodes were assembled into 2032-type coin cells using lithium disc as both the counter and reference
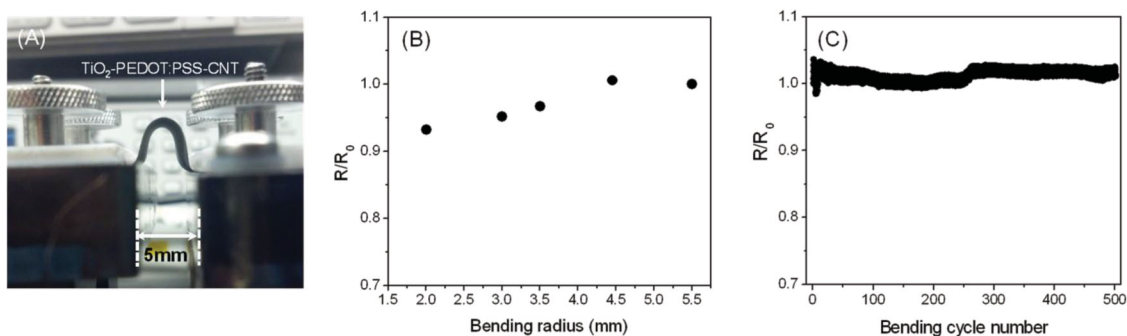
Figure 3. A) Photograph showing a TiO$_2$-PEDOT:PSS-CNT film with a bending radius of 2.0 mm. B) Change in film resistance under different bending conditions. C) Dependence of film resistance over 500 bending cycles with a bending radius of 3.5 mm (resistance was normalized).

electrodes. For comparison, similar electrodes were made with a slurry consisting poly(vinylidene fluoride) (PVDF, a common binder for lithium battery electrodes, 15%), TiO$_2$ (60%) and CNT (25%). Figure S3 (Supporting Information) shows the morphology of the resulting electrode, which is highly porous and composed of large aggregates, suggesting that TiO$_2$ particles and CNTs were not uniformly dispersed. Electrochemical impedance spectroscopy study was first conducted and the obtained Nyquist plots at open circuit voltage (OCV) for both electrodes are shown in **Figure 4**A. For electrodes with similar mass loadings, the TiO$_2$-PEDOT:PSS-CNT electrode has a significantly lower charge transfer resistance than that of TiO$_2$-PVDF-CNT electrode (30 vs. 100 Ohm), suggesting that the conducting polymer network effectively decreased the electrode resistance as compared to the traditional non-conductive

binder. We note that this merit is not only attributed to the high conductivity of PEDOT:PSS, but also from a better dispersion of TiO$_2$ nanoparticles and CNT in the precursor solution. In addition, both electrodes show a 45° Warburg tail in the low frequency range, which indicates a semi-infinite diffusion process and is commonly observed for lithium electrodes.

Cyclic voltammetric experiments were carried out at different sweep rates (0.5 to 50 mV s^{-1}) to evaluate the charge storage capacity and rate behavior (see Figure S4, Supporting Information). Figure 4B presents representative cyclic voltammograms (CV) at sweep rates of 0.5, 2 and 10 mV s^{-1}, respectively. The electrochemical Li$^+$ insertion/extraction processes occurring at anatase TiO$_2$ electrode can be expressed by:

$$TiO_2 + xLi^+ + xe^- \leftrightarrow Li_xTiO_2$$
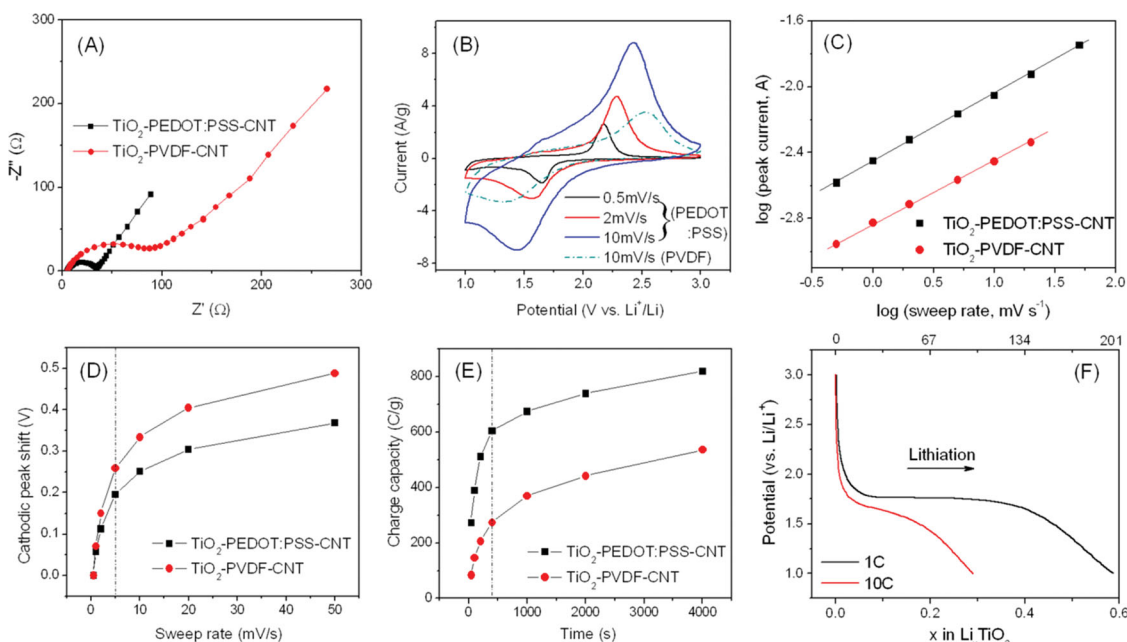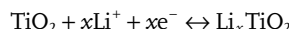
Figure 4. A) Comparison of impedance spectrum (Nyquist plot) of TiO$_2$-PEDOT:PSS-CNT and TiO$_2$-PVDF-CNT electrodes at OCV. B) CV plots of a representative flexible TiO$_2$-PEDOT:PSS-CNT electrode at sweep rate of 0.5, 2 and 10 mV s^{-1}. A CV plot of a TiO$_2$-PVDF-CNT electrode at a sweep rate of 10 mV s^{-1} is inserted for comparison. C) The relationship between log-peak current and log-sweep rate and D) dependence of cathodic peak separation on the sweep rate of TiO$_2$-PEDOT:PSS-CNT and TiO$_2$-PVDF-CNT electrodes. E) Capacity dependence of each electrode on charging time. F) Galvanostatic charge curve of TiO$_2$-PEDOT:PSS-CNT electrode at constant rates of 1C and 10C.

where x is the mole fraction of the inserted lithium ions ($x \leq 1$).[39,40] For CV at 0.5 mV s^{-1}, two well-defined redox peaks are observed at 1.65 V (cathodic sweep) and 2.17 V (anodic sweep), corresponding to the biphasic transition between tetragonal anatase and orthorhombic lithium titanate and is consistent with typical insertion/extraction behavior of lithium in TiO$_2$.[34,39] As the sweep rate increases, these current peaks were retained, suggesting facile electrode kinetics. The CV curves with large symmetric under-curve areas at high sweep rates (e.g., 10 mV s^{-1}) indicated that a significant portion of the charge storage arises from surface reactions.[39] By comparison, the CV curve at 10 mV s^{-1} of TiO$_2$-PVDF-CNT electrode showed a much lower peak current and smaller under-curve area, suggesting a larger polarization and less charge storage capacity.

Quantitative analysis provided a better understanding on the kinetics of different electrodes. Figure 4C presents a plot of log (i) versus log (v) from 0.5 to 50 mV s^{-1} for TiO$_2$-PEDOT:PSS-CNT (Figure S4, Supporting Information). The peak at 50 mV s^{-1} was severely distorted for TiO$_2$-PVDF-CNT electrodes due to strong polarization, thus peaks from only 0.5 to 20 mV s^{-1} were considered (Figure S5, Supporting Information). Generally, the peak current obeys a power-law as governed by $i = av^b$, where a and b are adjustable values.[41] A b value of 0.5 or 1 would suggest that charge current was controlled by semi-infinite linear diffusion or surface reaction, respectively.[39] The b values for PEDOT:PSS- and PVDF-based electrodes are 0.42 and 0.38, respectively, thus confirming a semi-infinite diffusion process. These values were less than 0.5 possibly due to thick electrodes where polarization from active material resistance, ohmic contact, pore diffusion resistance, etc. played a large role.[42] A higher b value for the former electrode indicates its less polarization characteristics. Consistently, TiO$_2$-PEDOT:PSS-CNT electrode showed a smaller peak voltage shift than that of TiO$_2$-PVDF-CNT electrodes at all sweep rates (Figure 4D), which again verified its better kinetics.

As a result, PEDOT:PSS-based composite electrode delivered more charge under all our studied conditions. Figure 4E shows the capacity dependence on charging time. TiO$_2$-PEDOT:PSS-CNT electrode showed a capacity 820 C g^{-1} (or 227 mAh g^{-1}) at 0.5 mV s^{-1} (corresponding to a charge/discharge time of 4000 s), significantly higher than that of TiO$_2$-PVDF-CNT electrode (537 C g^{-1} or 149 mAh g^{-1}). According to galvanostatic charge/discharge measurements, the maximum capacity was ≈230 mAh g^{-1} at a rate of C/3 (Figure S6, Supporting Information), which was close to our obtained CV test result. Similar CV testing with a PEDOT:PSS-CNT electrode, in absence of active nanoparticles, indicated that the conductive components showed negligible charge capacity (Figure S7, Supporting Information). The maximum areal capacity was observed to reach 0.37 mAh cm^{-2}, which is significantly higher than previously reported values obtained with thin-film TiO$_2$ electrodes. For example, Hammond et al.[35] recently reported an aqueous-based layer-by-layer electrostatic self-assembly approach to fabricate thin film TiO$_2$/CNT electrodes. The electrodes showed a similar gravimetric capacity and high-rate capability to TiO$_2$-PEDOT:PSS-CNT at a small thickness of ≈1.5 μm, and also resulted in an areal capacity of less than 50 μAh cm^{-2}.[35] This value was approximately one order of magnitude smaller than our flexible TiO$_2$ composite electrodes. Moreover, the other advantage of

high packing density is the capability to deliver high volumetric capacity. Along with high density of the composite film, the volumetric capacity was observed to reach 1.3 mAh cm^{-3}. Previous TiO$_2$ electrodes are often based on highly porous structures, thus the volumetric capacity was significantly lower.[38]

At a very fast sweep rate of 50 mV s^{-1} (charge/discharge in 40 s), the PEDOT:PSS-based electrode still retained a considerable capacity of 273 C g^{-1} (or 76 mAh g^{-1}), which is more than three times of the capacity for PVDF-based electrode (85 C g^{-1} or 24 mAh g^{-1}). Figure 4F shows the representative galvanostatic charge curves for TiO$_2$-PEDOT:PSS-CNT electrodes at a rate of 1 and 10 C (1C = 170 mA g^{-1}), respectively. At slower charge rate of 1 C, the curve shows a clear plateau at 1.75 V. This is due to the biphasic transition as indicated from CV test, and this part contributed a capacity of 101 mAh g^{-1}. The following sloping region also showed a capacity of 100 mAh g^{-1}, which is mainly from the interfacial lithium storage occurring on the small nanoparticles.[43] At a 10 C rate, the plateau region is absent and the charge capacity (97 mAh g^{-1}) was attributed to a sloping region, indicating better kinetics from the dominating interfacial reaction. Therefore, the high rate capacity obtained from TiO$_2$-PEDOT:PSS-CNT electrodes was due to the good retention of interfacial capacity and is thus not diffusion limited. Correspondingly, it was reasoned that the loss of major capacity for TiO$_2$-PVDF-CNT was mainly because of a low conductivity in the bulk electrode. These comparative studies indicated that the use of PEDOT:PSS to construct a highly conductive electrode can enable high rate performance at high mass loading.

Besides significantly improving rate capability, the PEDOT:PSS-CNT hydrogel network can also enhance the cycling stability of high-capacity anode materials, and to tolerate large volume change during repeated cycling processes. Using Si nanoparticles (SiNPs), we also demonstrated that the interpenetrating PEDOT:PSS-CNT network can allow us to fabricate highly stable Si anode for high energy flexible lithium ion battery. Among the many candidates for high energy lithium anode, Si has been considered as the most promising one.[26] However, Si-based anodes nonetheless have several drawbacks, such as ≈300% volume expansion upon lithium insertion, which results in fracture and loss of electrical contacts and unstable solid-electrolyte-interphase (SEI) growth on the Si surface. These issues often result in a short cycle life (i.e., only a few cycles) of bulk Si electrodes. Most current research efforts have focused on designing nanostructured or hybrid electrodes to mitigate these problems.[26,44] Making flexible Si electrodes using similar strategies also remains unsuccessful. Recent studies suggest that SiNPs can be used to fabricate electrodes by using the slurry processes, which are potentially compatible with current battery manufacturing route.[45–48] However, these SiNP electrodes are usually thin and non-flexible. Another major limitation is that their areal capacity is usually low (<0.5 mAh cm^{-2}), making them less attractive for practical applications. Using our above described approach in making TiO$_2$-PEDOT:PSS-CNT electrode (see Experimental Section), we successfully demonstrated the fabrication of flexible Si-PEDOT:PSS-CNT electrodes with good cycling stability and high areal capacity reaching 2.2 mAh cm^{-2}.

Figure 5A shows a SEM image of Si-PEDOT:PSS-CNT film electrode. The inset shows a digital photograph of a film

www.MaterialsViews.com

ADVANCED
ENERGY
MATERIALS

www.advenergymat.de

FULL PAPER
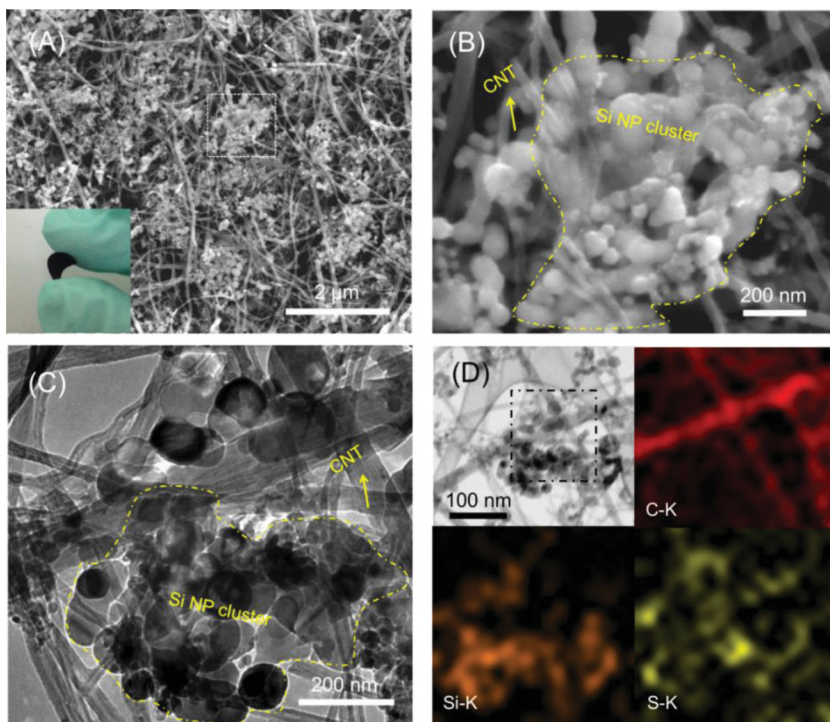
Figure 5. A) Low and B) high magnification SEM images of the top surface view of a representative Si-PEDOT:PSS-CNT film electrode. The CNT network penetrates through the whole film and SiNPs form clusters that are embraced by CNT pathways. C) TEM image of the composite film showing SiNPs clusters and CNT network. D) Elemental mapping showing the distribution of CNT, PEDOT:PSS and SiNPs (upper-left: spectrum image scanning, upper-right: C-K mapping, bottom-left: Si-K mapping, bottom-right: S-K mapping).

electrode with good flexibility. The SiNPs have a relatively broad size distribution, mainly in between 50 to 200 nm. Similar to TiO_2-PEDOT:PSS-CNT, a CNT network penetrating through SiNP clusters can clearly be observed. Figure 5B displays the high-magnification SEM image of the selected area in Figure 5A. A single Si cluster is observed to be threaded by multiple CNTs. Each SiNP is bound and coated by a glue-like layer, which we consider to be a PEDOT:PSS coating (Figure S8, Supporting Information). The TEM image in Figure 5C shows the intimate threading between CNT network and SiNP cluster and is again consistent with Figure 5B. Elemental mapping in Figure 5D clearly reveals the distribution of CNT, SiNP and PEDOT:PSS, indicated by C-K, Si-K and S/C-K mapping, respectively. The larger area indicated by S than Si suggests the wrapping of PEDOT:PSS onto the SiNPs. This is slightly different from the distribution of S in TiO_2-PEDOT:PSS-CNT, in which a more uniform spread of PEDOT:PSS was observed. This may be attributed to the smaller particle sizes of TiO_2 as compared to the SiNP (30 vs. 50–200 nm).

The lithium storage performance of Si-PEDOT:PSS-CNT was also evaluated using coin cells. The electrodes have a mass loading of ≈2 mg cm^{-2}, which contained 57% of SiNPs. **Figure 6**A shows first five CV
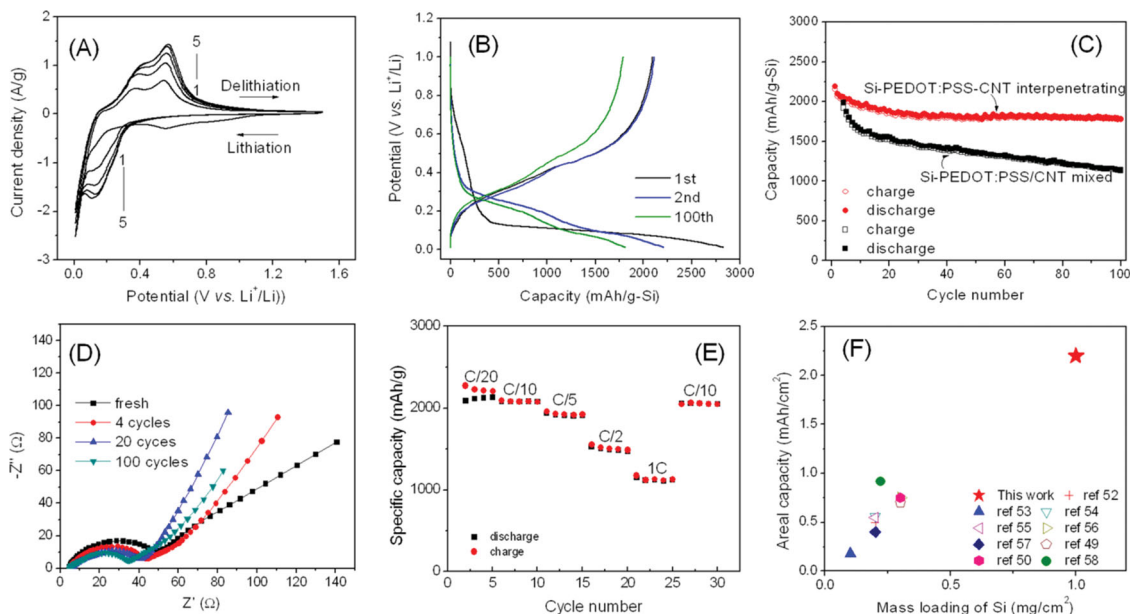
Figure 6. A) CV plots of a representative flexible Si-PEDOT:PSS-CNT electrode at a sweep rate of 0.2 mV s^{-1} on the first 5 cycles. B) 1st, 2nd and 100th cycle galvanostatic charge/discharge curve of an electrode at C/10. C) Cycling stability of a thick Si-PEDOT:PSS-CNT electrode at C/10 rate. Cycling result of a control electrode made by simply mixing Si-PEDOT:PSS with CNT is also presented. Areal capacity is also presented. D) Nyquist plots of Si-PEDOT:PSS-CNT electrode at OCV on fresh electrode and after 4th, 20th, and 100th cycle. E) Rate performance of the Si-PEDOT:PSS-CNT electrode electrodes. F) Comparison of areal capacity between the flexible Si-PEDOT:PSS-CNT electrode and other SiNP-based or nanostructured Si electrodes reported recently.

cycles of a typical electrode at a potential sweep rate of 0.2 mV s^{-1}. The cathodic peak at 0.56 V on the first CV curve is due to the SEI layer formation on the relatively high surface area electrode (CNT and Si). This peak disappeared in the following cycles, indicating good stability of such SEI layers. The voltammetric current associated with the formation of Li-Si alloy began at ≈0.33 V and increased rapidly below 0.2 V, which is accompanied by the formation of different phases of $Li_{12}Si_7$ and $Li_{15}Si_4$, respectively. Two anodic peaks (at 0.35 V and 0.55 V) appeared on discharge curve, corresponding to the conversion of amorphous Li_xSi to Si. The increase of charge current with cycling can be attributed to a gradual activation of more active SiNPs embedded in the thick electrode. Such a CV feature is consistent with many previously reported Si structures.[26,49,50]

Figure 6B presents galvanostatic charge/discharge plots on 1st, 2nd and 100th cycle at a constant rate of C/10. The voltage profile for the first discharge cycle showed a long flat plateau, where crystalline Si reacted with lithium to form amorphous Li_xSi. A capacity of 2820 mAh g^{-1} (based on the mass of Si) was achieved during this process. The first discharge capacity was 2180 mAh g^{-1}, corresponding to a coulombic efficiency of 77.3%. We note that the capacity from PEDOT:PSS-CNT in the voltage window of 0.01 to 1 V is also negligible (95 mAh g^{-1}), when compared with SiNPs (Figure S9, Supporting Information). The following charge and discharge cycles showed different characteristic voltage profiles, which may be due to the de-lithiation and lithiation of amorphous Li_xSi and Si, respectively.[26] The second cycle discharge capacity decreased to 2209 mAh g^{-1}, but the columbic efficiency was increased to 95.6%. Both the charge and discharge capacities remained stable during the subsequent cycles and a charge capacity of 1802 mAh g^{-1} was obtained after 100 cycles. The capacity dependence on cycle number was shown in Figure 6C, in which cycling performance of an electrode made by mixing CNT with PEDOT:PSS coated SiNP was compared. The flexible Si-PEDOT:PSS-CNT electrode kept ≈90% of its initial capacity while the later electrode lost ≈55% of its capacity. This could be easily understood since the hybrid hydrogel electrodes contain uniformly distributed CNT and intimate polymer wrapping around each component, while the control electrodes contain some large Si-PEDOT aggregates (Figure S10, Supporting Information) and worse dispersed CNT. These drawbacks cause a poor Si-CNT interface, which tends to lose electrical conductivity more easily during cycling, leading to worse cycling performance. In addition, previous work in using SiNP-PEDOT:PSS composite electrode with carboxymethyl cellulose binder only showed a Si capacity of ≈1200 mAh g^{-1}, along with 35% loss after 80 cycles.[51] SEM images (Figure S11, Supporting Information) of the electrodes after charge/discharge cycling show a well-retained CNT network. The PEDOT:PSS and Si NPs cannot be clearly identified due to large structural changes and transformation of crystalline SiNP into amorphous Si, but the cluster-like structures threaded by CNT was preserved. This result reaffirmed the structural advantages in our construction of a mechanically stable 3D interpenetrating PEDOT:PSS-CNT network, in which the SiNPs were effectively confined within a robust conductive framework to enable stable cycling.

Electrochemical impedance measurements provided further evidence on the stability of the Si-PEDOT:PSS-CNT electrode during repeated cycling processes. Figure 6D shows the Nyquist plots of the electrodes at different cycling status at OCV. Each plot consists of a semicircle at high frequency range and a Warburg tail at low frequency range. The former is due to electrolyte resistance and charge-transfer resistance, while the latter represents diffusion-resistance from electrode materials. Using the same cell, a decrease in the semicircle during cycling indicates increased electrode conductivity and composite interface during lithiation and de-lithiation. The change of the slope in the Warburg tails was due to a combined effect between the increase of electrode porosity and growth of SEI layer. Overall, the retained small electrode series resistance confirmed the high robustness of the PEDOT:PSS-CNT network. Besides, the electrodes also displayed good rate capability due to the high conductivity retained under charge/discharge cycling. As shown in Figure 6E, the electrode was able to preserve a capacity of ≈1200 mAh g^{-1} at a rate of 1C (or 4.2 A g^{-1}). This high rate capability is comparable with other SiNP-based electrodes with much less mass loading.[49,50]

Real application of batteries requires electrodes with a high areal capacity since the inert components (e.g., current collector, separator) contribute a significant part of the whole cell. Importantly, our unique interpenetrating Si-PEDOT:PSS-CNT electrode architecture enabled a high real capacity which has yet been achieved with previously reported SiNP electrodes. As shown in Figure 6C, the areal capacity reached 2.2 mAh cm^{-2} with the initial cycle and retained to 1.8 mAh cm^{-2} during the following 100 cycles. By comparison, previous SiNP and common nanostructured Si electrodes often have an areal capacity of less than 1 mAh cm^{-2} (Figure 6F),[49,50,52–58] which was approximately one fold lower than our electrodes. For example, our group has previously reported ultra-long cycling SiNP electrodes by conformal coating of conductive polyaniline (PAni) on SiNPs, but the areal capacity was only about 0.7 mAh cm^{-2} (due to the relatively low conductivity of PAni).[49] Recently, Yu et al. reported a 3D hierarchical ternary SiNP composite electrode using polypyrrole (PPy) and single-walled CNT as conductive additives.[50] They achieved stable cycling of 1000 cycles, but suffered in its low areal capacity (0.4–0.7 mAh cm^{-2}). Since our electrodes were constructed by a robust hydrogel network of long-CNT and PEDOT:PSS, they were able to maintain high electronic conductivity through the bulk electrodes during cycling. Thus, both high mass loading and high areal capacity can simultaneously be achieved. The realization of such high areal capacity SiNP electrodes using CNT-conducting polymer hydrogel network opens great opportunities to fabricate flexible, light-weight and high-energy lithium battery for practical applications.

3. Conclusions

In summary, we have successfully developed an aqueous-based solution process for efficient fabrication of high performance flexible lithium electrodes using a synergistic combination of conducting polymer solution, CNTs and nanoparticle building blocks. The resulting interpenetrating network of CNT-conducting polymer hydrogels provided good mechanical properties, high conductivity and facile ion transport, thus leading to

www.MaterialsViews.com

ADVANCED
ENERGY
MATERIALS
www.advenergymat.de

FULL PAPER

facile electrode kinetics and high strain tolerance during volumetric changes. Due to these structural merits, we are able to achieve high-rate capability for TiO$_2$ and high cycling stability for SiNP electrodes. Both electrodes also showed high gravimetric capacity and high areal capacity, greatly surpassing previously reported nanostructured electrodes with the same active materials. This simple yet efficient solution process thus provides a promising route towards fabrication of a variety of high performance flexible electrodes. By optimally coupling both the anode and cathode active materials, we envision that flexible high rate supercapacitors and high energy lithium battery can hence be afforded for practical applications.

4. Experimental Section

Fabrication of Flexible TiO$_2$-PEDOT:PSS-CNT and Si-PEDOT:PSS-CNT Electrodes: To make a flexible TiO$_2$-PEDOT:PSS-CNT film, a hybrid hydrogel was first prepared. Typically, commercial TiO$_2$ nanoparticles (20 mg, Degussa P25, diameter ≈30 nm, 95% anatase phase) were dispersed in DI-water (5 mL) by sonication and stirring. 1.2% PEDOT:PSS solution (0.4 mL, Clevios PH1000) and superlong-CNTs (10 mg) were added to the above dispersion to make a hydrogel precursor. After mixing for 2 h, APS solution (1 mL, 0.2 g mL^{-1}) was added to above precursor solution. In about 5 min, the solution became viscous and gel-like, indicating a hydrogel formation. The hydrogel was further dispersed under stirring by adding 5 mL of DI-water. After stirring for another 2 h, the solution was filtrated with a nylon filter paper (pore size 0.45 μm) using vacuum filtration and washed by DI-water, leading to a flat film on the filter paper. The film was dried under ambient condition and then peeled off from the filter paper. To make electrodes, the film was punched into desired sizes and dried at 80 °C under vacuum for 3 h. The film thickness can be easily tuned by changing the amount of the precursor solution, and a typical mass loading of TiO$_2$-PEDOT:PSS-CNT composite materials was ≈2.8 mg cm^{-2}. The electrode density was calculated based on the mass loadings and thickness of the active layers by assuming a bulk density of 2.2, 1.0 and 4.3 g cm^{-3} for CNT, PEDOT:PSS and TiO$_2$, respectively. Si-PEDOT:PSS-CNT electrodes were fabricated in the same way by replacing TiO$_2$ with SiNPs. For control study, PEDOT:PSS-CNT film was made without adding any inorganic particles into the precursor solution.

Si-PEDOT:PSS/CNT Mixture: To make a mixed Si-PEDOT:PSS/CNT electrodes, a Si-PEDOT:PSS hydrogel was prepared by the same process described above but without adding CNT in the hydrogel precursor. After Si-PEDOT:PSS hydrogel was obtained, CNT was added with stirring and the mixed solution was filtered and washed to obtain a film.

Fabrication of TiO$_2$-PVDF-CNT Electrodes: A slurry-coating process was used to fabricate TiO$_2$-PVDF-CNT electrodes. P25 TiO$_2$ powder, CNT and PVDF binder were mixed in a mass ratio of 6:2.5:1.5 and homogenized in *N*-methyl-2-pyrrolidone (NMP) to form slurries. The homogenous slurries were coated on Cu foil substrates and dried at 80 °C for 2 h under vacuum. As-formed electrodes were then calendered and further dried under vacuum at 80 °C for another 12 h. The mass loading was controlled to be 2.5–3 mg cm^{-2}.

Material Characterization: SEM experiments were conducted on an FEI XL30 Siron SEM with FEG source. To see the real morphology, the Si-cycled PEDOT:PSS-CNT electrodes were washed with acetone followed by 0.1 M HCl to remove the surface SEI layer before imaging. TEM experiments were carried out on a FEI Tecnai G2 F20 X-TWIN operated at 200 kV. Bending test was conducted on a home-made bending/stretching test station. To evaluate electrochemical performance, 2032-type coin cells were assembled in an argon-filled glovebox, using Celgard 2500 membrane as the separator. Lithium discs were used as both the counter and reference electrodes, and 1 M LiPF$_6$ in ethylene carbonate/diethylcarbonate/vinylene carbonate (1:1:0.02 v/v/v, Ferro Corporation) was used as the electrolyte. The CV and electrochemical impedance spectroscopy measurement were performed on a Bio-Logic

VMP3 electrochemical workstation. The Nyquist plots were recorded potentiostatically by applying an AC voltage of 10 mV amplitude in the frequency range of 0.01–100 kHz. Galvanostatic charge/discharge test was conducted on an Arbin 2000 multi-channel battery tester. All electrochemical measurements were carried out at room temperature.

Supporting Information

Supporting Information is available from the Wiley Online Library or from the author.

Acknowledgements

[1] H. Nishide, K. Oyaizu, *Science* **2008**, *319*, 737.
[2] V. L. Pushparaj, M. M. Shaijumon, A. Kumar, S. Murugesan, L. Ci, R. Vajtai, R. J. Linhardt, O. Nalamasu, P. M. Ajayan, *Proc. Natl. Acad. Sci. USA* **2007**, *104*, 13574.
[3] L. Hu, J. W. Choi, Y. Yang, S. Jeong, F. La Mantia, L.-F. Cui, Y. Cui, *Proc. Natl. Acad. Sci. USA* **2009**, *106*, 21490.
[4] M. Koo, K.-I. Park, S. H. Lee, M. Suh, D. Y. Jeon, J. W. Choi, K. Kang, K. J. Lee, *Nano Lett.* **2012**, *12*, 4810.
[5] L. Hu, H. Wu, F. La Mantia, Y. Yang, Y. Cui, *ACS Nano* **2010**, *4*, 5843.
[6] Y. H. Kwon, S.-W. Woo, H.-R. Jung, H. K. Yu, K. Kim, B. H. Oh, S. Ahn, S.-Y. Lee, S.-W. Song, J. Cho, H.-C. Shin, J. Y. Kim, *Adv. Mater.* **2012**, *24*, 5192.
[7] X. Jia, Z. Chen, A. Suwarnasarn, L. Rice, X. Wang, H. Sohn, Q. Zhang, B. M. Wu, F. Wei, Y. Lu, *Energy Environ. Sci.* **2012**, *5*, 6845.
[8] K. Wang, W. Zou, B. Quan, A. Yu, H. Wu, P. Jiang, Z. Wei, *Adv. Energy Mater.* **2011**, *1*, 1068.
[9] A. M. Gaikwad, A. M. Zamarayeva, J. Rousseau, H. Chu, I. Derin, D. A. Steingart, *Adv. Mater.* **2012**, *24*, 5071.
[10] L. Yuan, X.-H. Lu, X. Xiao, T. Zhai, J. Dai, F. Zhang, B. Hu, X. Wang, L. Gong, J. Chen, C. Hu, Y. Tong, J. Zhou, Z. L. Wang, *ACS Nano* **2012**, *6*, 656.
[11] Y.-H. Lee, J.-S. Kim, J Noh, I. Lee, H. J. Kim, S. Choi, J. Seo, S. Jeon, T.-S. Kim, J.-Y. Lee, J. W. Choi, *Nano Lett.* **2013**, *13*, 5753.
[12] L. Nyholm, G. Nyström, A. Mihranyan, M. Strømme, *Adv. Mater.* **2011**, *23*, 3751.
[13] C. Meng, C. Liu, S. Fan, *Electrochem. Commun.* **2009**, *11*, 186.
[14] Q. Wu, Y. Xu, Z. Yao, A. Liu, G. Shi, *ACS Nano* **2010**, *4*, 1963.
[15] C. Wang, W. Zheng, Z. Yue, C. O. Too, G. G. Wallace, *Adv. Mater.* **2011**, *23*, 3580.
[16] J. Wang, C. Y. Wang, C. O. Too, G. G. Wallace, *J. Power Sources* **2006**, *161*, 1458.
[17] L. Yuan, B. Yao, B. Hu, K. Huo, W. Chen, J. Zhou, *Energy Environ. Sci.* **2013**, *6*, 470.
[18] Y. Meng, Y. Zhao, C. Hu, H. Cheng, Y. Hu, Z. Zhang, G. Shi, L. Qu, *Adv. Mater.* **2013**, *25*, 2326.

[19] K. Wang, Q. Meng, Y. Zhang, Z. Wei, M. Miao, *Adv. Mater.* **2013**, *25*, 1494.

[20] Y. Cheng, S. Lu, H. Zhang, C. V. Varanasi, J. Liu, *Nano Lett.* **2012**, *12*, 4206.

[21] A. Sumboja, C. Y. Foo, X. Wang, P. S. Lee, *Adv. Mater.* **2013**, *25*, 2809.

[22] Y. Meng, K. Wang, Y. Zhang, Z. Wei, *Adv. Mater.* **2013**, *25*, 6985.

[23] M. Kaempgen, C. K. Chan, J. Ma, Y. Cui, G. Gruner, *Nano Lett.* **2009**, *9*, 1872.

[24] F. Liu, S. Song, D. Xue, H. Zhang, *Adv. Mater.* **2012**, *24*, 1089.

[25] D. Deng, M. G. Kim, J. Y. Lee, J. Cho, *Energy Environ. Sci.* **2009**, *2*, 818.

[26] C. K. Chan, H. Peng, G. Liu, K. Mcilwrath, X. F. Zhang, R. A. Huggins, Y. Cui, *Nat. Nanotechnol.* **2008**, *3*, 31.

[27] Y. Xia, J. Ouyang, *J. Mater. Chem.* **2011**, *21*, 4927.

[28] D. Alemu, H.-Y. Wei, K.-C. Ho, C.-W. Chu, *Energy Environ. Sci.* **2012**, *5*, 9662.

[29] J. E. Yoo, K. S. Lee, A. Garcia, J. Tarver, E. D. Gomez, K. Baldwin, Y. Sun, H. Meng, T.-Q. Nguyen, Y.-L. Loo, *Proc. Natl. Acad. Sci. USA* **2010**, *107*, 5712.

[30] S. Razdan, P. K. Patra, S. Kar, L. Ci, R. Vajtai, A. Kukovecz, Z. Kónya, I. Kiricsi, P. M. Ajayan, *Chem. Mater.* **2009**, *21*, 3062.

[31] E. M. Hotze, T. Phenrat, G. V. Lowry, *J. Environ. Qual.* **2010**, *39*, 1909.

[32] W. Zhang, B. Zhao, Z. He, X. Zhao, H. Wang, S. Yang, H. Wu, Y. Cao, *Energy Environ. Sci.* **2013**, *6*, 1956.

[33] D. Antiohos, G. Folkes, P. Sherrell, S. Ashraf, G. G. Wallace, P. Aitchison, A. T. Harris, J. Chen, A. I. Minett, *J. Mater. Chem.* **2011**, *21*, 15987.

[34] T. Brezesinski, J. Wang, J. Polleux, B. Dunn, S. H. Tolbert, *J. Am. Chem. Soc.* **2009**, *131*, 1802.

[35] M. N. Hyder, B. M. Gallant, N. J. Shah, Y. Shao-Horn, P. T. Hammond, *Nano Lett.* **2013**, *13*, 4610.

[36] I. Abayev, A. Zaban, F. Fabregat-Santiago, J. Bisquert, *Physica Status Solidi (a)* **2003**, *196*, R4.

[37] R. Asmatulu, A. Karthikeyan, D. C. Bell, S. Ramanathan, M. J. Aziz, *J. Mater. Sci.* **2009**, *44*, 4613.

[38] K. Saravanan, K. Ananthanarayanan, P. Balaya, *Energy Environ. Sci.* **2010**, *3*, 939.

[39] J. Wang, J. Polleux, J. Lim, B. Dunn, *J. Phys. Chem. C* **2007**, *111*, 14925.

[40] M. Wagemaker, W. J. H. Borghols, F. M. Mulder, *J. Am. Chem. Soc.* **2007**, *129*, 4323.

[41] H. Lindstrom, S. Sodergren, A. Solbrand, H. Rensmo, J. Hjelm, A. Hagfeldt, S.-E. Lindquist, *J. Phys. Chem. B* **1997**, *101*, 7717.

[42] V. Augustyn, J. Come, M. A. Lowe, J. W. Kim, P.-L. Taberna, S. H. Tolbert, H. D. Abruña, P. Simon, B. Dunn, *Nat. Mater.* **2013**, *12*, 518.

[43] J.-Y. Shin, D. Samuelis, J. Maier, *Adv. Funct. Mater.* **2011**, *21*, 3464.

[44] A. Magasinski, P. Dixon, B. Hertzberg, A. Kvit, J. Ayala, G. Yushin, *Nat. Mater.* **2010**, *9*, 353.

[45] L. B. Hu, H. Wu, S. S. Hong, L. F. Cui, J. R. McDonough, S. Bohy, Y. Cui, *Chem. Commun.* **2011**, *47*, 367.

[46] H. Kim, B. Han, J. Choo, J. Cho, *Angew. Chem. Int. Ed.* **2008**, *47*, 10151.

[47] G. Liu, S. Xun, N. Vukmirovic, X. Song, P. Olalde-Velasco, H. Zheng, V. S. Battaglia, L. Wang, W. Yang, *Adv. Mater.* **2011**, *23*, 4679.

[48] H. Wu, G. Y. Zheng, N. A. Liu, T. J. Carney, Y. Yang, Y. Cui, *Nano Lett.* **2012**, *12*, 904.

[49] H. Wu, G. Yu, L. Pan, N. Liu, M. T. McDowell, Z. Bao, Y. Cui, *Nat. Commun.* **2013**, *4*, 1943.

[50] B. Liu, P. Soares, C. Checkles, Y. Zhao, G. Yu, *Nano Lett.* **2013**, *13*, 3414.

[51] L. Yue, S. Wang, X. Zhao, L. Zhang, *J. Mater. Chem.* **2012**, *22*, 1094.

[52] Y. Yao, M. T. McDowell, I. Ryu, H. Wu, N. Liu, L. Hu, W. D. Nix, Y. Cui, *Nano Lett.* **2011**, *11*, 2949.

[53] H. Wu, G. Chan, J. W. Choi, I. Ryu, Y. Yao, M. T. McDowell, S. W. Lee, A. Jackson, Y. Yang, L. Hu, Y. Cui, *Nat. Nanotechnol.* **2012**, *7*, 310.

[54] N. Liu, K. Huo, M. T. McDowell, J. Zhao, Y. Cui, *Sci. Rep.* **2013**, *3*, 1919.

[55] B. Wang, X. Li, X. Zhang, B. Luo, Y. Zhang, L. Zhi, *Adv. Mater.* **2013**, *25*, 3560.

[56] M.-H. Ryou, J. Kim, I. Lee, S. Kim, Y. K. Jeong, S. Hong, J. H. Ryu, T.-S. Kim, J.-K. Park, H. Lee, J. W. Choi, *Adv Mater.* **2012**, *25*, 1571.

[57] X. Zhou, A.-M. Cao, L.-J. Wan, Y.-G. Guo, *Nano Res.* **2012**, *5*, 845.

[58] M. Wu, X. Xiao, N. Vukmirovic, S. Xun, P. K. Das, X. Song, P. Olalde-Velasco, D. Wang, A. Z. Weber, L.-W. Wang, V. S. Battaglia, W. Yang, G. Liu, *J. Am. Chem. Soc.* **2013**, *135*, 12048.

wileyonlinelibrary.com